Archive of Applied Mechanics (2023) 93:663–685
https://doi.org/10.1007/s00419-022-02292-1

ORIGINAL

G. Pepe · A. Doria · N. Roveri · A. Carcaterra

Vibration energy harvesting for cars: semi-active piezo controllers

Received: 12 May 2020 / Accepted: 11 October 2022 / Published online: 25 October 2022

Abstract Energy harvesting represents one of the recent challenging subjects related to vibration and control. The scale of energy harvesters and storage can involve a wide power range, and the scale of some milliwatt is the elective field of piezoelectric applications. This paper investigates the power frontiers of the piezoelectric-based harvesters applied to automotive units. The analysis, supported by experimental data, aims at estimating the upper bound of the specific power of this technology for powering small devices on board cars. Passive optimally tuned piezoelectric harvester and semi-active controlled ones are compared, based on a new control strategy named VFC-Variational Feedback Control, recently developed by the authors. This new technique makes it possible to increase the total energy storage drained from car vibrations. However, the real advantage for their use relies on a sharp balance between the harvested power and the costs for the additional hardware mass transport. Numerical simulations of circuitry and experimental vibration data provides references to assess the energy convenience in installing this type of devices on board.

Keywords Energy harvesting · Car vibrations · Piezoelectric · Optimal control theory · Variational control · Nonlinear control · Nonlinear model predictive control

1 Introduction

Nowadays piezoelectric devices are widely used for scavenging energy from ambient vibrations. The main advantages of piezoelectric materials in energy harvesting stand in the large power density and the no need for external power sources.

Several studies have investigated the power output of a harvester excited by a fixed frequency vibration source. The results show, as intuitive, the generated power can be maximized when the natural frequency of the harvester is tuned on the vibration frequency and when the electrical load is set to an optimum value [1, 2]. Both experimental and numerical results [3] have revealed the existence of two characteristic natural frequencies related to the harvester, one is the short circuit resonance frequency, the other is the open circuit natural frequency. The difference between these frequencies becomes important when the electromechanical

G. Pepe (✉) · N. Roveri · A. Carcaterra
Department of Mechanical and Aerospace Engineering, Sapienza University of Rome, Rome, Italy
e-mail: gianluca.pepe@uniroma1.it

N. Roveri
e-mail: nicola.roveri@uniroma1.it

A. Carcaterra
e-mail: antonio.carcaterra@uniroma1.it

A. Doria
Department of Industrial Engineering, University of Padova, Padua, Italy
e-mail: alberto.doria@unipd.it

coupling coefficient is large [4]. Optimal values of a purely resistive load that maximizes power output at the two typical resonances can be found in [3]. Some researchers extended the investigation considering more realistic electrical loads, which include the AC-DC converter [4–6]. In this case, optimal values of the load impedance can maximize the power output.

These analyses show that a suitable variation of the load impedance can compensate for the decrease in the generated power when the excitation frequency moves away from the resonance condition. Hence, it is possible to collect a relevant amount of power in the frequency bandwidth about the resonances [7].

The performance of a simple passive harvester with a given load impedance is poor when the source of excitation is characterized by broadband and/or variable spectrum. Sources like these are rather common in many engineering systems. In vehicles, the spectrum of vibrations caused by tire-road interaction and by the engine forces shows many components changing in time, because of the different engine/motor rotational speed variations and the different road roughness [8]. In large structures (e.g., bridges and buildings) vibrations due to traffic and to wind have broadband and variable spectra [9].

Two approaches have been proposed to improve the power output of piezo harvesters in the presence of broadband and/or variable spectra. The first consists of widening the band of operation of the passive harvester modifying the mechanical sub-system. Many solutions have been proposed in recent years [10], and they are based on harvester arrays [11–13], trimming devices [14], complex harvester geometries [1, 15–17], and exploitations of nonlinear effects [18–23].

The second approach consists of the development of harvesters equipped with adaptive circuits, which take into account the vibration spectrum and can modify their load impedance [7]. An adaptive AC-DC rectifier, able to adjust the output voltage according to the vibration amplitude, is described in [24], to achieve the maximum power transfer. A good review of adaptive circuits for maximizing power output is presented in [25]. Recently, some active circuits are designed to increase both the generated power and frequency bandwidth. In particular, in [26], a tunable synchronous electric charge extraction interface is illustrated. It increases the frequency bandwidth about the resonance in which a significant amount of power can be harvested. In [27], a power processing circuit, equipped with an artificial neural network, can set the impedance connected to the harvester to its optimum value.

In this paper, the energy harvested by a cantilever piezo harvester installed in a car is boosted by employing a new controller based on the Variational Feedback Control (VFC) strategy. VFC controllers have been recently used to improve the performance of semi-active car suspensions [28–30] and to control other complex systems [31–34]. The potentialities of this control strategy in the field of vibration energy harvesting have been highlighted in [35], which adopted a general approach suited to electromagnetic, piezoelectric, and capacitive harvesting.

One of the key elements to assess a real beneficial use of the vibration harvesters relies on the estimate of the power they can supply, compared with the additional costs the presence of the harvesters imply. In fact, the harvester introduces an additional hardware on board, and the transport of this extra-weight has its cost. On the other hand, the harvester can be placed very close, because of its small dimensions, to the energy user unit, with the beneficial effect of reducing the cables weight. This technical important argument will be discussed in the conclusions, after the main figures about the extracted power from the device are analyzed in depth along the paper. In particular, the estimate of an upper bound for the extracted power is of interest to produce a reference value. However, the control method to extract the maximum power, based on NMPC-Nonlinear Model Predictive Control, shows a too complex algorithm that could only run on sophisticated electronic boards (meaning large weights), and with computational times that are not compatible with the time response of the device. An alternative solution of much more practical use is the VFC algorithm that can perform an optimization with respect to the purely passive harvester, but with a very simple and very light electronics.

The paper is organized as follows. The mathematical model of a cantilever piezoelectric harvester is presented in Sect. 2. The equation of motion is solved with the modal decomposition approach and the maximum power that can be drained by the passive harvester equipped with the optimal resistive load is calculated. The parameters of the model are finely tuned in Sect. 3 making use of experimental tests carried out with the impulsive method. The main features of the VFC are summarized in Sect. 4. The application of the VFC strategy to the load resistance of a cantilever harvester mounted on a car is presented in Sect. 5. Numerical simulations are carried out considering actual acceleration inputs measured onboard a small city car, see Fig. 1. Numerical results show the VFC strategy makes it possible to double the energy storage with respect to the passive solution, and that it is able to extract more than one third of the maximum energy absorbed by a NMPC that knows the future disturbance. Finally, conclusions are drawn in Sect. 6.

(a) (b)

Fig. 1 SMART Fortwo of Vehicle System Dynamic and Mechatronic Laboratory of Sapienza: **a** the vehicle; **b** the testing equipment

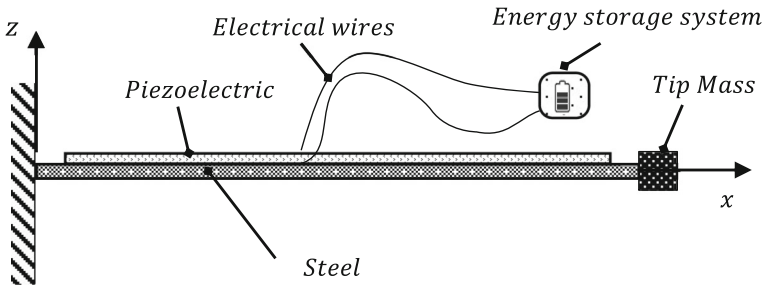

Fig. 2 Clamped-free piezo-harvester

2 Model of the piezoelectric harvester

In this section, the model of a cantilever piezoelectric beam harvester, shown in Fig. 2, is developed as a reference to evaluate the performance of the VFC controller. The analytical model below is based on the Euler–Bernoulli model for bending beam with clamped–free boundary conditions and a tip mass rigidly attached at the free end. This model is based on the characteristics of a PPA 1001 harvester manufactured by Midé [36], whose characteristics are listed in Table 1. It is a unimorph harvester of rectangular shape and size compatible with automotive applications (41.1 × 20.8 mm). The active piezo layer is made of PZT 5H, whereas the structural layer is made of stainless steel. The piezo material satisfies the following constitutive equation [1]:

$$\begin{Bmatrix} T_1 \\ D_3 \end{Bmatrix} = \begin{bmatrix} c_{11} & -e_{31} \\ e_{31} & \varepsilon_{33} \end{bmatrix} \begin{Bmatrix} S_1 \\ E_3 \end{Bmatrix} \tag{1}$$

where D_3, E_3, T_1 and S_1 are the electric displacement, the electric field, stress, and strain, respectively and:

$$\begin{aligned} \varepsilon_{33} &= \varepsilon_{33}^T - d_{31}^2 c_{11} \\ e_{31} &= d_{31} c_{11} \end{aligned} \tag{2}$$

where ε_{33}^T, c_{11} and d_{31} are the dielectric constant under constant stress, the piezo Young's modulus and the piezoelectric constant, respectively. Figure 3 shows the nomenclature of the main dimensions used for the model. Note the piezo exhibits symmetry about the z axis, which is the poling axis of the material.

The equation of a controlled piezo-beam system is derived from Hamilton's principle:

$$\delta J = \int_{t_1}^{t_2} (\delta T + \delta W + \delta W_{nc}) \mathrm{d}t = 0 \tag{3}$$

Table 1 General proprieties of the piezo-beam system

Material properties	Value
Piezo dimensions $l_p \times h_p \times b\ (mm)$	$46 \times 0.23 \times 20.8$
Piezo density $\rho_p\ (kg/m^3)$	7800
Piezo Young's modulus $c_{11} = 1/s_{11}^E\ (GPa)$	60
Piezoelectric constants $e_{31}\left(\frac{C}{m^2}\right)$	-10
Permittivity constant $\varepsilon_{33}\ \left(\frac{nF}{m}\right)$	27.486
Beam density $\rho_b\ (kg/m^3)$	7800
Beam dimensions l_b x h_b x $b\ (mm)$	46 x 0.23 x 20.8
Young's modulus $Y\ (GPa)$	60
Integral eigenfunction $\Psi_1 = \int_0^l \phi_1(x)dx$ [without tip mass; 3 g of tip mass; 16 g of tip mass]	$[-0.5922; -0.2833; -0.1351]$
Eigenfunction derivative $\phi_1^{'}(l)$ [without tip mass; 3 g of tip mass; 16 g of tip mass]	$[-984.1; -504.97; -246.12]$
Eigenfunction $\phi_1(l)$ [without tip mass; 3 g of tip mass; 16 g of tip mass]	$[-32.64; -16.02; -7.69]$
Natural frequency $f_1(Hz)$ [without tip mass; 3 g of tip mass; 16 g of tip mass]	[125; 60; 28]
Damping factor ζ_1	0.01
Optimal Resistance R (k¨) [without tip mass; 3 g of tip mass; 16 g of tip mass]	[12; 23; 57]

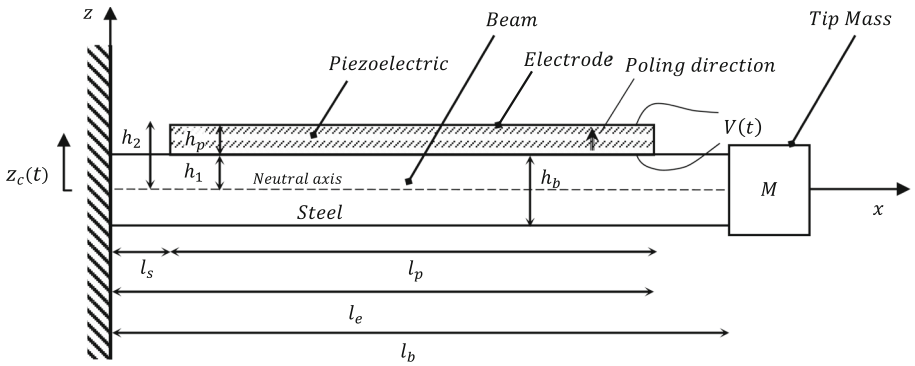

Fig. 3 Main dimensions of the harvester

with T kinetic energy, W co-energy function and W_{nc} non-conservative energy:

$$\begin{aligned} T &= \frac{1}{2}\int_0^l (\rho A + M\delta(x-l))\dot{w}(x,t)^2 \mathrm{d}x \\ W &= \frac{1}{2}\int_0^l \mathrm{d}x \int_A \left(\varepsilon_{33} E_3^2 \tilde{H}(x) + 2e_{31} E_3 S_1 \tilde{H}(x) - c_{11} S_1^2 \tilde{H}(x) - Y S_1^2\right)\mathrm{d}A \end{aligned} \tag{4}$$

where $S_1 = -zw^{''}$ is the strain along x-axes, $w(x,t)$ and $\widetilde{H}(x) = H(x-l_s) - H(x-l_e)$ are the displacement along the x-axis and a window function with edges at the extremes of the piezo layer, respectively. l_b, l_p are the length of the beam and the length of the piezo (see Fig. 3), M is the tip mass located at $x = l_b$ and Y is the beam Young's modulus. Furthermore, $\rho A = \rho_p A_p \widetilde{H}(x) + \rho_b A_b$ where ρ_p, ρ_b, A_p and A_b are the piezo and beam density, and their cross-section area, respectively.

The virtual work of non-conservative forces is:

$$\delta W_{nc} = \int_0^l p(x,t)\delta w \mathrm{d}x - Q(t)\delta V(t) \tag{5}$$

where $p(x,t)$ and $Q(t)$ are the distributed transverse load applied to the beam and the charge over the piezo layer, respectively. $E_3 = -\frac{V(t)}{h_p}$ is the spatial uniform electrical field along the piezo, and $V(t)$ is the voltage between the electrodes. The Hamiltonian principle returns:

$$\begin{aligned}
&\rho A\ddot{w} + \left[-e_{31}h_m bV(t)\tilde{H}(x) + \left(c_{11}I_p\tilde{H}(x) + YI_b\right)w''\right]'' = p(x,t)\\
&\frac{\varepsilon_{33}bl_p}{h_p}\dot{V}(t) + \dot{Q}(t) + e_{31}h_m b\dot{w}'\Big|_{l_s}^{l_e} = 0\\
&\text{with boundary conditions :}\\
&\left[-e_{31}h_m bV(t)\tilde{H}(x) + \left(c_{11}I_p\tilde{H}(x) + YI_b\right)w''\right]\delta w'\Big|_0^l = 0\\
&\left[-e_{31}h_m bV(t)\tilde{H}(x) + \left(c_{11}I_p\tilde{H}(x) + YI_b\right)w''\right]'\delta w\Big|_0^l - M\ddot{w}\,\delta w|_l = 0
\end{aligned} \tag{6}$$

where $h_m = \frac{(h_2+h_1)}{2}$, $I_p = \frac{bh_p^3}{12} + bh_p h_m^2$, $I_b = \frac{bh_b^3}{12}$, $h_p = h_2 - h_1$, $h_b = 2h_1$ and h_1, h_2 are geometrical thickness shown in Fig. 3, while b is the width of the piezo-beam.

The beam vertical displacement is expressed as:

$$w(x,t) = z_c(t) + w_{el}(x,t) \tag{7}$$

where $z_c(t)$ is the base vertical vibration (assumed integral with the car structure), as shown in Fig. 3, and $w_{el}(x,t)$ is the elastic beam vertical displacement with respect to the base. Accordingly, Eq. (6) become:

$$\begin{aligned}
&\rho A\ddot{w}_{el} + \left[\left(c_{11}I_p\tilde{H}(x) + YI_b\right)w_{el}''\right]'' = p(x,t) - (\rho A + M\delta(x-l))\ddot{z}_c + e_{31}h_m bV(t)\tilde{H}''(x)\\
&\frac{\varepsilon_{33}bl_p}{h_p}\dot{V}(t) + \dot{Q}(t) + e_{31}h_m b\dot{w}_{el}'\Big|_{l_s}^{l_e} = 0\\
&w_{el}(0,t) = w_{el}'(0,t) = 0\\
&w_{el}''(l,t) = 0\ ;\left(c_{11}I_p + YI_b\right)w_{el}'''(l,t) - M\ddot{w}_{el}(l,t) = 0
\end{aligned} \tag{8}$$

where clamped-free boundary conditions are considered.

Modal decomposition transforms Eq. (8) into a set of ordinary differential equations [1, 37]:

$$w_{el}(x,t) = \sum_r^{\infty}\phi_r(x)\eta_r(t) \tag{9}$$

$\phi_r(x)$ is the rth mass-normalized eigenfunction and $\eta_r(t)$ the rth modal coordinate. If ($l_p = l$) and considering the case with a generic impedance R, shown in Fig. 4, the equations become:

$$\begin{cases}
\ddot{\eta}_r(t) + \dot{\eta}_r(t)2\zeta_r\omega_r + \eta_r(t)\omega_r^2 = \int_0^l \phi_r\Big[p(x,t) - (\rho(x)A + M\delta(x-l))\ddot{z}_c + e_{31}h_m bV(t)\tilde{H}''(x)\Big]\text{with } r = 1\ldots n\\
C_p\dot{V}(t) + \frac{V(t)}{R} + e_{31}h_m b\sum_r^{\infty}\phi_r'(l)\dot{\eta}_r(t) = 0
\end{cases} \tag{10}$$

where $C_p = \frac{\varepsilon_{33}bl_p}{h_p}$ is the capacitance of the piezo, ζ_r is the damping factor and it takes into account some forms of dissipation, $\omega_r^2 = \frac{(c_{11}I_p+YI_b)}{\rho AL^4}\lambda_r^4$ are the natural frequencies of the beam and λ_r is the associated natural wavenumbers, that in the case of beam with mass at the end is obtained by solving the following expression [37, 38]:

$$1 + \cos\lambda_r\cosh\lambda_r + \lambda_r\frac{M}{\rho Al}(\cos\lambda_r\sinh\lambda_r - \sin\lambda_r\cosh\lambda_r) = 0 \tag{11}$$

Furthermore, considering the piezoelectric is here modelled to store energy, the derivative of the charge is $\dot{Q}(t) = \frac{V(t)}{R}$, i.e., the piezo is connected to an electrical circuit with an impedance R which will be constant in case of a passive absorber and will be variable R for a semi-active absorber, as later discussed. The second

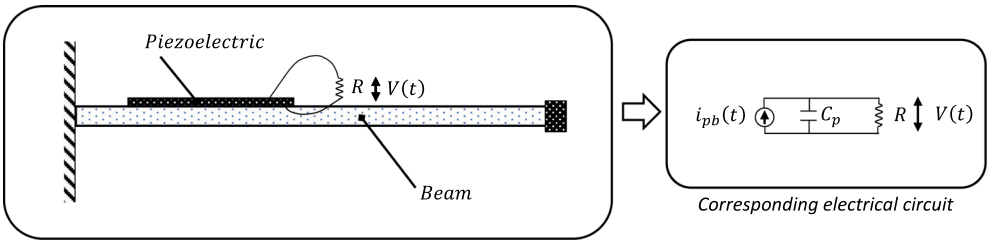

Fig. 4 Clamped-free piezo-harvester and corresponding electrical circuit

of Eq. (10) is represented in Fig. 4, in which the current generator $i_{pb}(t)$ represents the vibrating mechanical coupling.

In the passive case, the optimum resistive load R must be deduced by the maximum reference power extracted by the device from the base vibrations. In this contest, the distributed transverse load applied to the beam, for example, due to the gravity force, can be neglected without losing generality. The piezoelectric voltage $V(j\omega)$ is determined from Eq. (10) in the Fourier domain, and the drained power can be calculated as $P(j\omega) = \frac{|V(j\omega)|^2}{R}$:

$$P(j\omega) = \frac{1}{R}\left|\left(\frac{e_{31}h_m b\sum_r^{\infty}\left(\frac{j\omega\phi_r'(l)(\Psi_r\rho A+M\phi_r(l))}{(-\omega^2+j\omega 2\zeta_r\omega_r+\omega_r^2)}\right)}{\left((e_{31}h_m b)^2\sum_r^{\infty}\left(\frac{j\omega\phi_r'^2(l)}{(-\omega^2+j\omega 2\zeta_r\omega_r+\omega_r^2)}\right)+j\omega C_p+\frac{1}{R}\right)}\right)\right|^2 |A_c(j\omega)|^2 \tag{12}$$

where $A_c(j\omega) = -\omega^2 Z_c$. Then the optimal value of R is the one maximizing P over a frequency band $[f_1, f_2]$.

$$P_{\max} = \max_R \int_{2\pi f_1}^{2\pi f_2} P(j\omega)\mathrm{d}\omega \tag{13}$$

Let's start analyzing the maximum extractable power in the case of zero tip mass: for a frequency band around the first resonance [0, 300Hz] numerical maximization gives R $\sim$ 12 kΩ. Figure 5 shows, for several values of the resistive load, the power Frequency Response Function FRF $H_{Pow}(f)$, i.e., the ratio between the generated power $P(j\omega)$ and the second power of the base acceleration $|A_c(j\omega)|^2$, predicted by the numerical model, taking into account 3 vibration modes ($r = 3$). The resistive load has a large influence on the generated power both near the resonance and in between the resonances.

Since the resonance peaks are well separated, the study of the behavior of the harvester about the first resonance (125 Hz) can be done considering only the first mode response in the model . The results of Fig. 6 indicate the value R = 12k¨ optimizes the generated power. Figure 7 depicts the maximum power harvested P_{max} of Eq. (13) in the frequency band around the first resonance [0; 300Hz] for different values of the resistive load when the vertical acceleration is a white Gaussian noise.

3 Experimental tests

For a single-mode response, two coupled equations follow from the Eq. (10), with the values reported in Table 1:

$$\begin{aligned}\ddot{\eta}_1(t) + \dot{\eta}_1(t)2\zeta_1\omega_1 + \eta_1(t)\omega_1^2 &= -(\Psi_1\rho A + M\phi_1(l))\ddot{z}_c + \phi_1'(l)e_{31}h_m bV(t)\\ C_p\dot{V}(t) + \frac{V(t)}{R} + e_{31}h_m b\phi_1'(l)\dot{\eta}_1(t) &= 0\end{aligned} \tag{14}$$

To corroborate the numerical results, the parameters of the model represented by Eqs. (14) and (10) have been tuned for the best fitting of experimental results carried on the commercial harvester PPA-1001 without tip mass [36].

Figure 8 shows the experimental setup for the measurement of the FRF between the voltage generated by the harvester and the base acceleration with the impulsive technique [39]. The harvester is clamped at one end of a stiff bar, which is excited by a hammer for modal testing at the opposite end. The duration of the

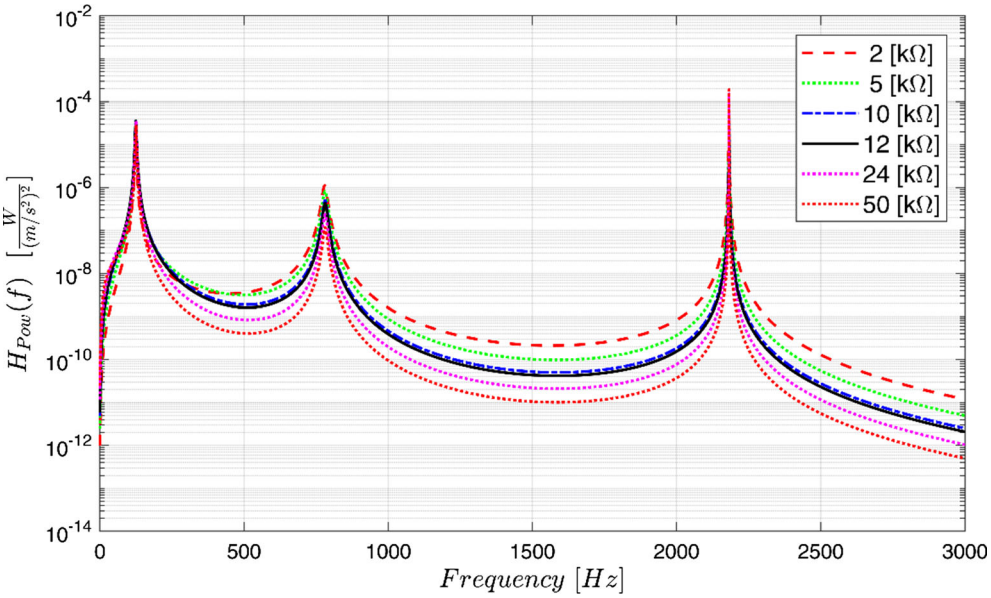

Fig. 5 Power FRF of the harvester considering three modes of vibration in the model ($r = 3$) and zero tip mass

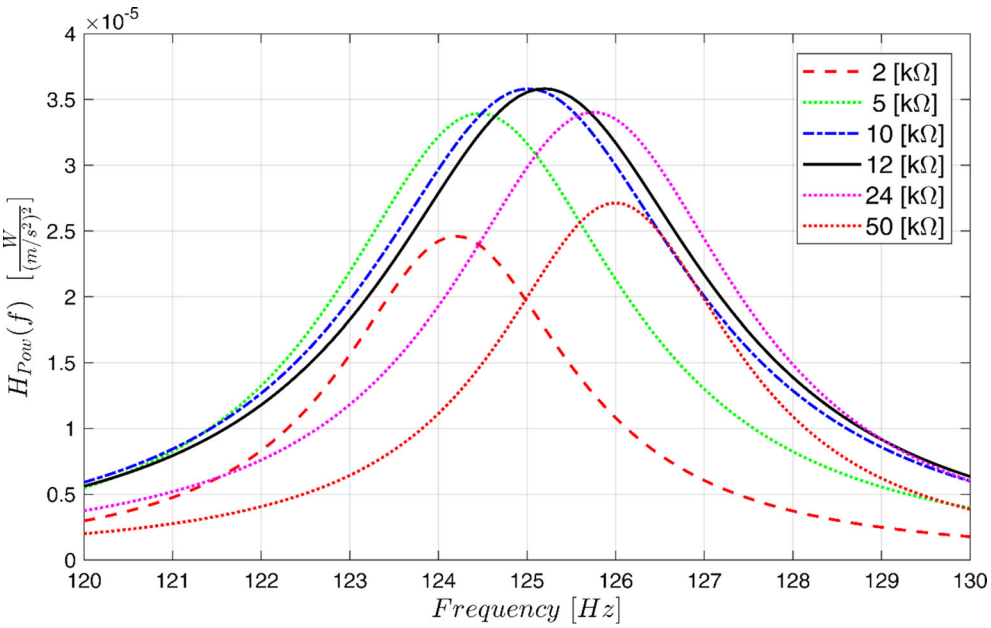

Fig. 6 Energy harvester frequency response considering zero tip mass

recorded signal is $3s$ and the sampling rate $4000\,Hz$. The FRF is calculated using a fast Fourier transform by the geometric mean of $H1$ and $H2$ estimators with a rectangular window. In this way, the longitudinal vibrations of the bar generated by the hammer hit excite the base of the harvester, whose vibrations are measured by a small accelerometer. The bar is suspended by a frame restrained by cables. This setup permits to decouple the resonant frequency of the piezo layer (occurring at about 120 Hz) from the very low natural frequency of the suspended bar (at about 2 Hz). The FRFs are measured for different resistive loads and for each resistive load three tests are carried out.

Figure 9 displays the comparison between the experimental FRFs and the numerical FRFs calculated after the model tuning. There is an overall good agreement between experimental results and numerical simulation. Only the third experiment carried out at 24kΩ is rather different from the others with the same resistance. It is apparent how the FRF modulus largely depends on the resistive load, with a frequency peak slightly decreasing

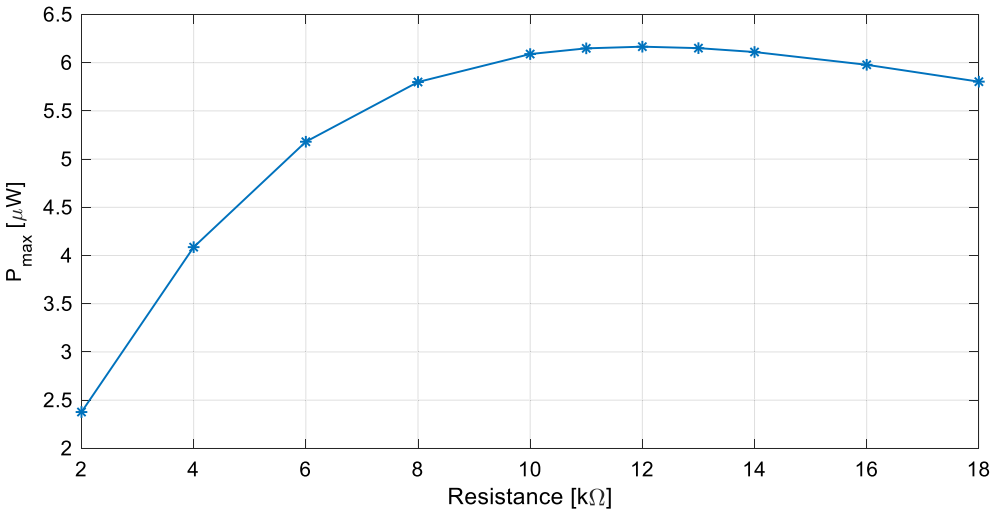

Fig. 7 Maximum power harvested by varying the electrical resistance in the passive case with Gaussian random excitation (standard deviation of vertical acceleration $2.5 m/s^2$) and zero tip mass

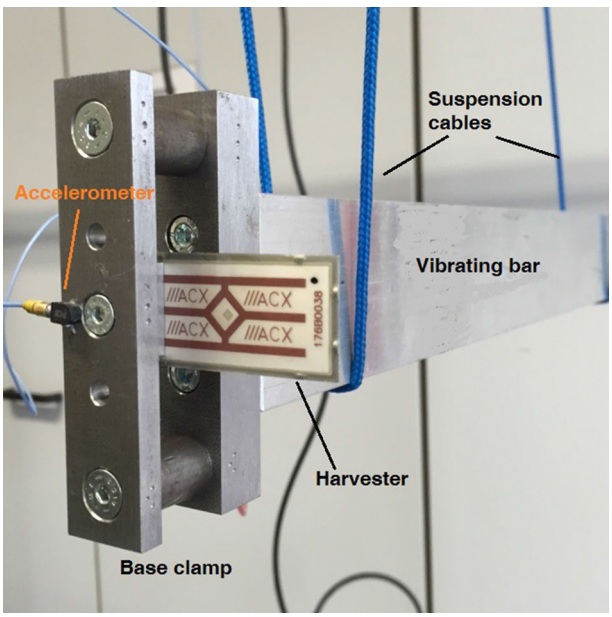

Fig. 8 Testing equipment with the suspended vibrating bar, the harvester and the accelerometer

with the decreasing of the resistive load. Eventually, Fig. 10 shows the generated power as a function of the resistance value for a set of frequencies within the range $123 - 127 Hz$. The amplitude of the mono-harmonic signal is 1 g. The discussed results demonstrate how the model represented by Eq. (14), with parameters given in Table 1, is a good reference to simulate the behavior of the typical piezo energy harvester.

In the following sections, this model is combined with a self-adapting resistor $R(t)$ made time-dependent through the use of a standard circuitry. In particular, the resistance value is controlled as a function of the voltage at the piezoelectrical terminals, which is obeying the control law recently introduced by the authors for semi-active mechanical suspension devices [28].

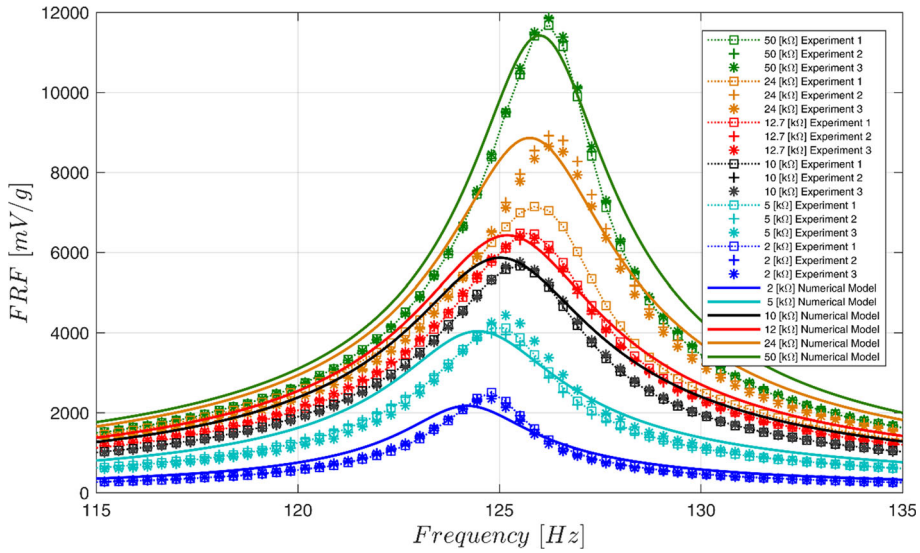

Fig. 9 Numerical VS Experimental FRF of PPA 1001 with different resistive loads

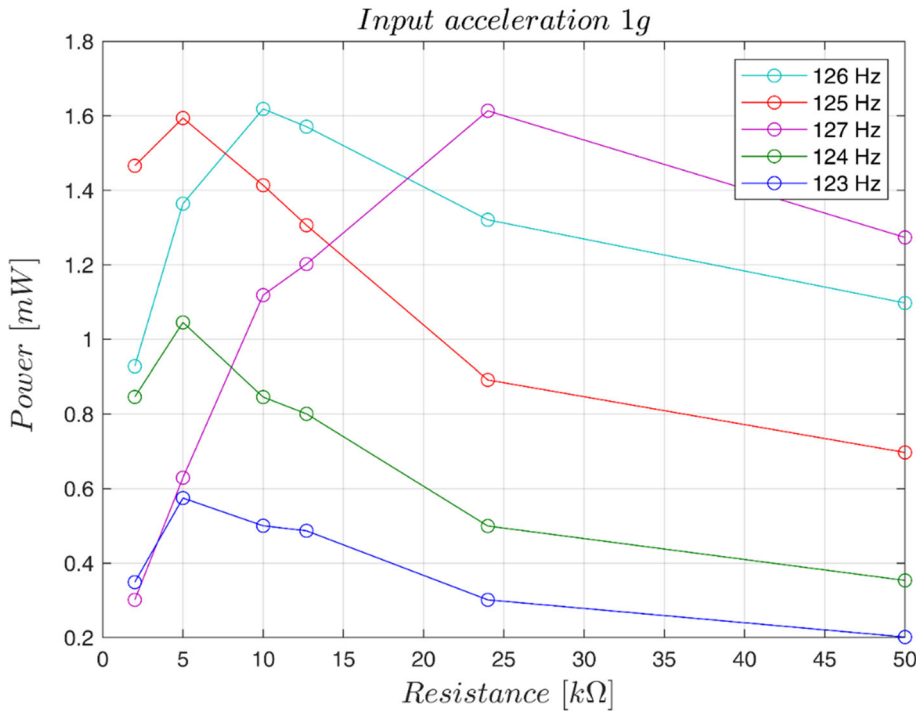

Fig. 10 Effect of load resistance on experimental powers at assigned frequencies

4 Harvester semi-active control

In this section, the strategy for semi-active control of the harvester is introduced, based on the Variational Feedback Control (VFC) [28, 31, 40–43], briefly reported below.

The VFC derives from the variational principle based on Pontryagin's method [28, 44]. In general, such procedure aims to minimize a cost function J in time domain, which is equal to the integral of an objective function L depending on the state $\boldsymbol{x}(t)$, the control $\boldsymbol{u}(t)$ and an external disturbance $\boldsymbol{y}(t)$:

$$\begin{cases} J = \int_{t_0}^{t_f} L(\boldsymbol{x}(t), \boldsymbol{u}(t), \boldsymbol{y}(t))dt : \underset{\boldsymbol{u}\in U}{Opt}\, J \\ \dot{\boldsymbol{x}}(t) = \boldsymbol{f}(\boldsymbol{x}(t), \boldsymbol{u}(t), \boldsymbol{y}(t)) \\ \boldsymbol{x}(t_0) = \boldsymbol{x}_{t_0} \end{cases} \tag{15}$$

where $\dot{\boldsymbol{x}} = \boldsymbol{f}(\boldsymbol{x}, \boldsymbol{u}, \boldsymbol{y})$ is the dynamic equation of the controlled dynamical system with initial condition $\boldsymbol{x}(t_0) = \boldsymbol{x}_{t_0}$ and $\boldsymbol{u} \in U$ represents the restraints for the control variable, related to the technical limitations of the employed actuators . The variational calculus permits to maximize/minimize J. The method of Lagrangian multipliers $\boldsymbol{\lambda}$ is used, leading to the following formulation:

$$\begin{cases} \delta\widetilde{J} = \delta\int_{t_0}^{t_f} L(\boldsymbol{f}(\boldsymbol{x}, \boldsymbol{u}, \boldsymbol{y}), \boldsymbol{y}) + \boldsymbol{\lambda}^T(\dot{\boldsymbol{x}} - \boldsymbol{f}(\boldsymbol{x}, \boldsymbol{u}, \boldsymbol{y}))\mathrm{d}t = 0 \\ \boldsymbol{x}(t_0) = \boldsymbol{x}_{t_0} \end{cases} \tag{16}$$

By operating the functional variations, the following Euler–Lagrange equations, and the associated transversality conditions are produced:

$$\begin{cases} \left(L_f - \boldsymbol{\lambda}\right)^{\boldsymbol{T}} \boldsymbol{f}_{\boldsymbol{x}} = \dot{\boldsymbol{\lambda}}^T \\ \left(L_f - \boldsymbol{\lambda}\right)^{\boldsymbol{T}} \boldsymbol{f}_{\boldsymbol{u}} = 0^T \\ \dot{\boldsymbol{x}} = \boldsymbol{f}(\boldsymbol{x}, \boldsymbol{u}, \boldsymbol{y}) \\ \boldsymbol{x}(t_0) = \boldsymbol{x}_{t_0} \\ \boldsymbol{\lambda}^{\boldsymbol{T}}\left(t_f\right)\delta\boldsymbol{x}(t_f) = 0 \end{cases} \tag{17}$$

where $\boldsymbol{f}_{\boldsymbol{x}} = \frac{\partial f_i}{\partial x_j}$ and $\boldsymbol{f}_{\boldsymbol{u}} = \frac{\partial f_i}{\partial u_j}$ are the Jacobian matrixes. The VFC restricts the family of functions to which L and $\boldsymbol{f}$ belong. In the present analysis, it is assumed:

$$L(\boldsymbol{f}, \boldsymbol{y}) = \boldsymbol{f}^T \boldsymbol{Q} \boldsymbol{f} + \boldsymbol{f}^T \boldsymbol{T} \boldsymbol{y} = \dot{\boldsymbol{x}}^T \boldsymbol{Q} \dot{\boldsymbol{x}} + \dot{\boldsymbol{x}}^T \boldsymbol{T} \boldsymbol{y} \tag{18}$$

where $\boldsymbol{Q}$ e $\boldsymbol{T}$ are gain matrices, whose coefficients are tuned to optimize the control law. Expression (18) represents a generalized state-rate quadratic form, $\dot{\boldsymbol{x}}^T \boldsymbol{Q} \dot{\boldsymbol{x}}$, completed by the bilinear form $\dot{\boldsymbol{x}}^T \boldsymbol{T} \boldsymbol{y}$ in terms of the state and the external action $\boldsymbol{y}$. The VFC control gives the chance to solve the Pontryagin's problem by feedback thanks to the special form of the objective function. A simpler quadratic form in terms of the state $\boldsymbol{q}$ can be determined by using the augmented state $\boldsymbol{q} = [\boldsymbol{x}, \boldsymbol{I}]^{\boldsymbol{T}}$, $\dot{\boldsymbol{I}} = \boldsymbol{x}$, with an associated dynamic equation $\dot{\boldsymbol{q}} = \boldsymbol{g}(\boldsymbol{q}, \boldsymbol{u}) = [\boldsymbol{f}, \boldsymbol{x}]^T$, that produces the new objective function:

$$L'(\boldsymbol{g}, \boldsymbol{y}) = \boldsymbol{q}^T \boldsymbol{Q}' \boldsymbol{q} + \boldsymbol{q}^T \boldsymbol{T}' \boldsymbol{y} \tag{19}$$

The equation of motion is of an affine-control type:

$$\boldsymbol{f}(\boldsymbol{x}, \boldsymbol{u}, \boldsymbol{y}) = \boldsymbol{\varphi}(\boldsymbol{x}, \boldsymbol{y}) + \boldsymbol{S}(\boldsymbol{x}, \boldsymbol{y}) \tag{20}$$

i.e., it is nonlinear in the state, but linear in the control. It is shown in [28] that the optimal solution $\boldsymbol{u}^*$ of the previous problem, defined by the functional (18) with the differential constraint (20), is set in the form:

$$\boldsymbol{u}^* = \left[\widetilde{\boldsymbol{Q}}\boldsymbol{S}(\boldsymbol{x}, \boldsymbol{y})\right]^+\left[-\widetilde{\boldsymbol{Q}}\boldsymbol{\varphi}(\boldsymbol{x}, \boldsymbol{y}) - \mathbf{T}\boldsymbol{y}\right] \tag{21}$$

where $\widetilde{\boldsymbol{Q}} = \boldsymbol{Q} + \boldsymbol{Q}^T$, and the symbol "+" indicates pseudo-inverse. To account for the control saturation, $\boldsymbol{u} \in U$, the control variable constraint is managed as follows:

$$\begin{cases} \boldsymbol{u}^* \in U \rightarrow \boldsymbol{u} = \boldsymbol{u}^* \\ \boldsymbol{u}^* \notin U \rightarrow \boldsymbol{u} = \boldsymbol{u}_{\partial U} \end{cases} \tag{22}$$

generally known as clipping technique where $\boldsymbol{u}_{\partial U}$ are the control values at the frontier of the space U.

5 Harvester performance estimation: coupling experimental data and numerical simulations

The state-space model associated with Eq. (14) according to (20) is:

$$\dot{\boldsymbol{x}} = \boldsymbol{\varphi}(\boldsymbol{x}, \boldsymbol{y}) + \boldsymbol{S}(\boldsymbol{x})u \tag{23}$$

where:

$$\boldsymbol{\varphi}(\boldsymbol{x}, \boldsymbol{y}) = \begin{bmatrix} 0 & 1 & 0 \\ -\omega_1^2 & -2\zeta_1\omega_1 & \phi_1^{'}(l)e_{31}h_m b \\ 0 & -\frac{e_{31}h_m b}{C_p}\phi_1^{'}(l) & 0 \end{bmatrix} \begin{bmatrix} \eta \\ \dot{\eta} \\ V \end{bmatrix} + \begin{bmatrix} 0 \\ -(\Psi_1\rho A + M\phi_1(l))\ddot{z}_c \\ 0 \end{bmatrix}; \boldsymbol{S}(\boldsymbol{x}) = \begin{bmatrix} 0 \\ 0 \\ -\frac{V}{C_p} \end{bmatrix}$$
$$\boldsymbol{x} = \begin{bmatrix} \eta \\ \dot{\eta} \\ V \end{bmatrix}; u = \frac{1}{R}; \boldsymbol{y} = \begin{bmatrix} 0 \\ -(\Psi_1\rho A + M\phi_1(l))\ddot{z}_c \\ 0 \end{bmatrix} \tag{24}$$

Using the explicit control solution (21), described in the previous section, Eq. (24) produces:

$$u^* = \frac{1}{R^*} = \frac{g_1 * \eta + g_2 * \dot{\eta} + g_3 * V + g_4 * \ddot{z}_c}{V} \tag{25}$$

that represents the optimal control law to maximize the performance of the harvester. The g_i constants are unknown tuning parameters that arise from a nonlinear combination of $\boldsymbol{Q}$ and $\boldsymbol{T}$ coefficients of Eq. (19).

The equivalent circuit of the optimally controlled piezo harvester is shown in Fig. 11, where the control parameter is $u^* = \frac{1}{R^*}$, i.e., a variable resistive load. This device is technically implementable using an operational amplifier circuitry and it can control the electrical impedance at any time.

The resistance value $R(t)$ is saturated by a simple clipping procedure as shown in the control diagram shown in Fig. 11:

$$\begin{cases} R = R_{\max} & if\, R^* \geq R_{\max} \\ R = R_{\min} & if\, R^* < R_{\min} \end{cases} \tag{26}$$

The semi-active control logic (25) together with the condition that $R(t) > 0$ ensures the stability of the controlled dynamic system because its effect will be to simply adjust the dissipated energy level.

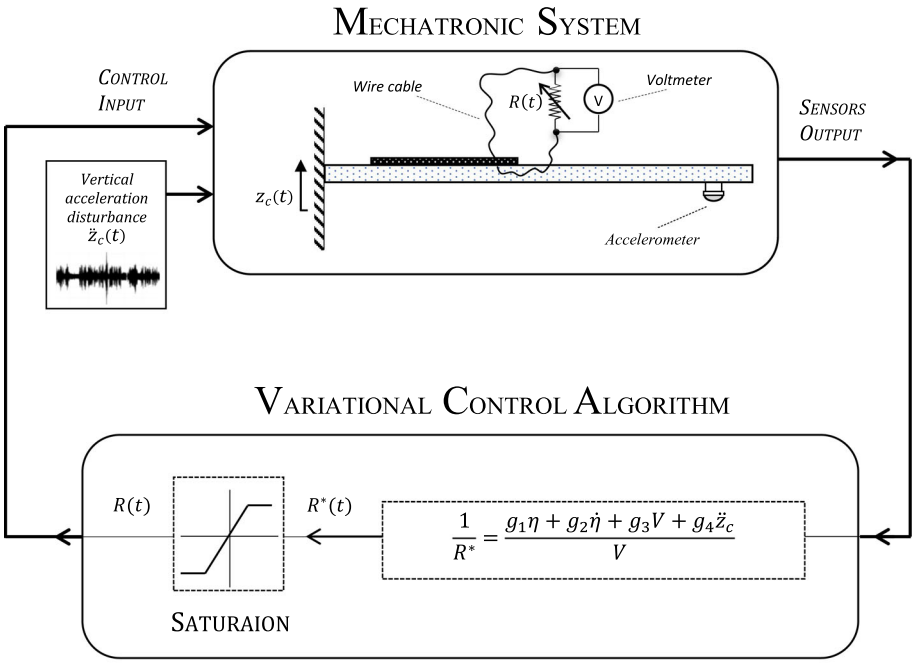

Fig. 11 VFC control diagram of the mechatronic system energy accumulator

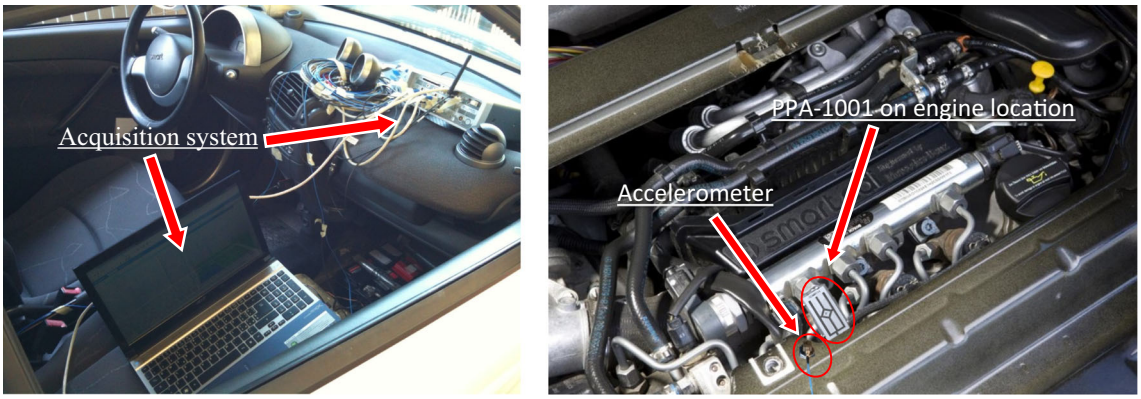

Fig. 12 Setup of the acquisition system (**a**); Piezo PPA-1001 on Smart Fortwo engine chassis with piezo accelerometer (**b**)

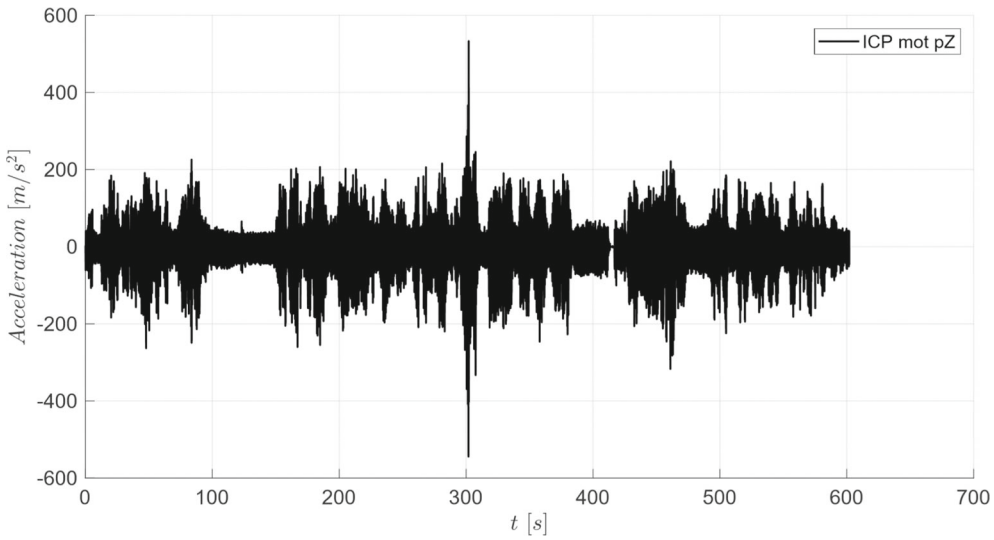

Fig. 13 Motor chassis acceleration of an extra-urban cycle for 10 min ride

The simulations are carried out considering acceleration values experimentally measured onboard one of the instrumented cars of the Vehicle System Dynamic and Mechatronic Laboratory of Sapienza. Figure 12 shows the experimental setup used to acquire the vertical vibration of the moving vehicle. The piezoelectric accelerometer, installed on the chassis near the main excitation point, i.e., the engine compartment, is acquired for almost 10 min of an extra-urban cycle. The accelerometer used has high sensitivity, 100 mV/g, and a max frequency band up to 10 kHz. In Fig. 13, a time record with a 20 kHz sample frequency of the measured acceleration is reported and in Fig. 14 a zoom of the power spectral density, to highlight the greatest oscillations occurs at low-frequency band [0–500] Hz is shown.

The power spectral density shows two important peaks: the first high and narrow about 28 Hz relative to the natural frequency of the combustion engine at neutral, while the second, wider located between 55 and 65 Hz, within which there are different frequencies: sub harmonics of the engine's main frequency, the local response of the chassis, and the road excitation (see Fig. 14). To increase the drained power, it is convenient glue a mass at the end of the beam to tune its fundamental natural frequency and the excitation frequency. For this reason, we compare two settings of tip mass: 3 g and 16 g, shifting the first natural frequency from 125 Hz, without mass, to 60 Hz and 28 Hz, respectively.

The advantage of adding mass is the increasing of the power transfer function. Figure 15 shows the trend of the integral of the power FRF evaluated by Eq. (12), between [0; 300Hz], depending on the choice of electrical resistance.

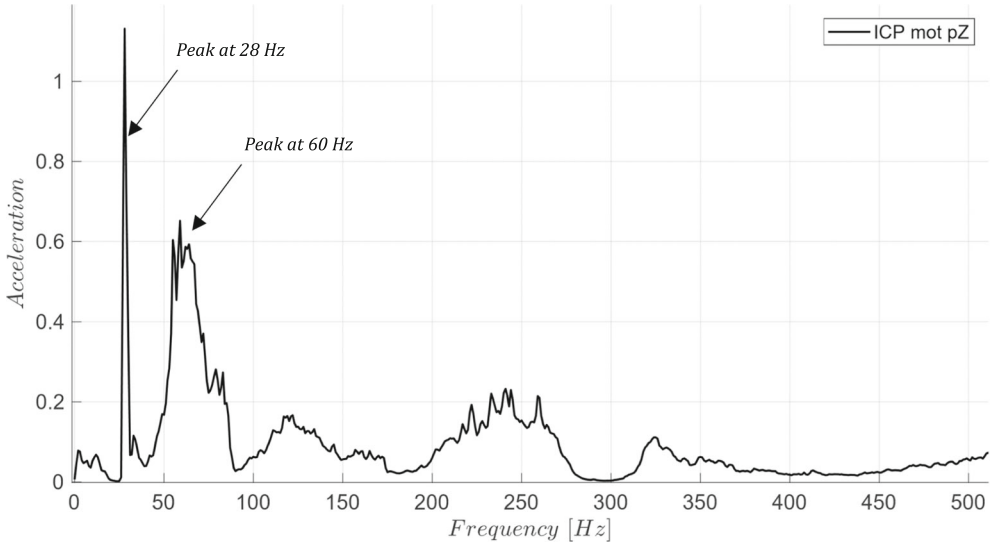

Fig. 14 Power spectral density (PSD) of motor chassis acceleration of an extra-urban cycle $\left[\left(\frac{m}{s^2}\right)^2/Hz\right]$

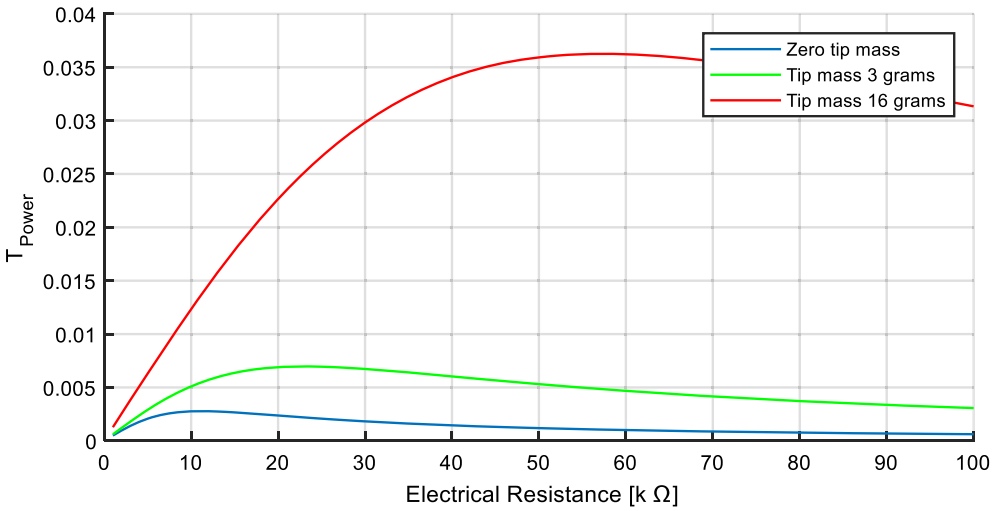

Fig. 15 Power transfer function, varying tip mass according to the electrical resistance

$$T_{Pow}(R) = \int_{f_1}^{f_2} H_{Pow}(f, R)\mathrm{d}f \tag{27}$$

For each chosen mass there is an optimal value of the electrical resistance that maximizes the power: 23 k Ω for 3 g and 57 k Ω for 16 g. This permits to obtain a gain factor equal to 10 of the transfer function response T_{Pow} changing the mass within the range 0–16 g.

Equation (25) represents the final form of the VFC used to maximize the electrical energy to be accumulated through the variation of the resistance of R. The gain parameters g_i are identified through the aid of an evolutionary algorithm called Genetic Algorithm (GA), i.e., a parametric optimization algorithm inspired by the Darwinian natural evolution [45]. The genetic algorithm has as objective function that of determining the optimal combination of the g_i unknown parameters for which the average accumulated energy is the highest possible. This was performed by imposing two types of control; a fast one, called *VFC case 1*, and a slow control *VFC*, named *case 2,* both supposing a single-mode response, numerically solving the Eq. (14). In the case of fast control, the simulation of the electromechanical model was performed by saturating the control

frequency up to 5 kHz while in the case of slow control the saturation reaches 1 kHz. The slow saturation is applied through the use of a first-order differential equation that simulates the delay time in the control response. Table 2 shows the g_i values found for both settings with added tip mass by the GA and the result of the objective function that is the mean harvested energy.

One can introduce a control technique that produces an upper bound for the energy absorbed, i.e., it plays as benchmark for comparison. This technique is the nonlinear model predictive control NMPC [46]. This type of control belongs to the category of optimal controls and is often used as a reference for comparison [47, 48]. Additionally, we assume, in the best case, the NMPC can know in advance all the future information about the disturbance $\boldsymbol{y}$. The NMPC is a variant of the model predictive control MPC [49] for which it is possible to treat dynamic systems and nonlinear constraints and nonquadratic objective functions. In general, most of the nonlinear optimal controls do not guarantee a priori an absolute minimum or maximum result, except for some singular and uncomplicated models that allow analytical solutions.

NMPC is applied by setting a finite predictive horizon time T_p from current time t, and at each predictive sample time Δt_s the predictive optimal control problem is solved over the entire range $[t; t+T_p]$ and determines future control values u over a control horizon T_c typically chosen as $T_c \leq T_p$. See Table 2 for the used simulation values.

The NMPC control maximizes a given cost function $\mathcal{L}(\boldsymbol{x}, u)$, in this case the integral of the power of the electrical circuit:

$$\max_{u} \mathcal{L}(\boldsymbol{x}, u) = \max_{R} \int_{t}^{t+T_p} \frac{(V(\tau))^2}{R(\tau)} \mathrm{d}\tau \tag{28}$$

with constraints represented by Eqs. (23) and (26), respectively:

$$\begin{gathered} \dot{\boldsymbol{x}}(\tau) = \boldsymbol{\varphi}(\boldsymbol{x}(\tau), \boldsymbol{y}(\tau)) + \boldsymbol{S}(\boldsymbol{x}(\tau))u(\tau), \ \forall \tau \in [t; t+T_p] \\ u(\tau) \in [u_{\min}; u_{\max}], \ \forall \tau \in [t; t+T_c] \\ u(\tau) = u(t+T_c), \ \forall \tau \in [t+T_c; t+T_p] \end{gathered} \tag{29}$$

In this particular case, the NMPC assumes that all the components of the state vector $\boldsymbol{x}(\tau)$areknown. Moreover, the future disturbance $\boldsymbol{y}(\tau)$, that is for example the acceleration $\ddot{z}_c(\tau)$, is also known $\forall \tau \in [t; t+T_p]$.

Figures 16 and 17 show the dynamic trends of piezoelectric controlled by the VFC logics. Figure 16 show the response of the piezoelectric in the presence of the tip added mass of 16 g while, in Fig. 17, the 3 g tip mass is considered.

For both cases a time zoom highlights how the different tuning of the VFC produce completely different behaviors. The *VFC case1* uses the g_2 tuning and the other gains zero, while the *VFC case 2* uses the g_1 parameter (see values shown in Table 2).

In Figs. 16a and 17a, the power shows a sequence of periodic large peaks for the *case1*, which are the distinctive elements of the semi-active control. The instant power at the peaks reaches the level of watts or tenths of watts, depending on the instant acceleration level. Instead, the power for *case2* is much smoother, approaching the continuous trends of the passive case.

The same trend occurs in Figs. 16c and 17c: the resistance varies impulsively with *case1* while in *case2* it is more continuous. Both resistance variations are saturated with a maximum value of $R_{\max} = 400\mathrm{k}^{\cdot\cdot}$ and a lower value $R_{\min}$ that does not drop below zero.

In Figs. 16b and 17b, the trend of the displacement at the end of the piezo is shown, and we can observe how the oscillations of the case with 3 g oscillate at a higher frequency but with smaller amplitudes than in the case with 16 g. *Case 1* produces a higher mitigation of the oscillations, absorbing a higher energy, with larger peaks in the current. *Case 2* shows a smoother trend of the current (see figures (d) and (e)).

Table 2 summarizes the results in terms of harvested energy, RMS of power and maximum displacement peak to peak reached for passive, VFC and NMPC cases. In general, the *VFC case 1* always extracts more energy than the *VFC case 2*, in fact it achieves an increase between 48 and 49% of stored energy relative to the passive case with 16 and 3 g added mass, respectively. Also, *case 1* shows a higher RMS power due to the high level of intermittency and indicates the technical realization of the circuitry does not need any continuously variable resistor, but a simpler on–off switch piloted by a transistor to load and unload a parallel resistor on the piezoelectric (see Fig. 18a). However, the intermittency requires that the energy storage management system is made up of fast capacitors to quickly collect the current circulating within the electrical circuit.

Table 2 Comparison of different control type: harvested energy, root mean square of the power and the maximum peak to peak displacement for 10 min of extra-urban cycle

Type of control	Tip mass [$gram$]	Control parameters	Harvested energy [J]	RMS power [mW]	Peak to peak displacement [mm]
Passive	3	$R = 23k\Omega$	0.24	2.47	6.3
	16	$R = 57k\Omega$	0.9	1.89	14.4
VFC case1	3	$g_2 = 30; g_1 = g_3 = g_4 = 0$	0.4	281.4	5.4
	16	$g_2 = 10; g_1 = g_3 = g_4 = 0$	1.67	77.9	12.6
VFC case2	3	$g_1 = -28; g_2 = g_3 = g_4 = 0$	0.37	4.16	4.8
	16	$g_1 = -3; g_2 = g_3 = g_4 = 0$	1.53	3.17	12.9
NMPC	3	$T_p = 3ms; T_c = 2ms; \Delta t_s = 1ms$	0.77	12.23	4.4
	16	$T_p = 3ms; T_c = 2ms; \Delta t_s = 1ms$	3.22	7.44	11.2

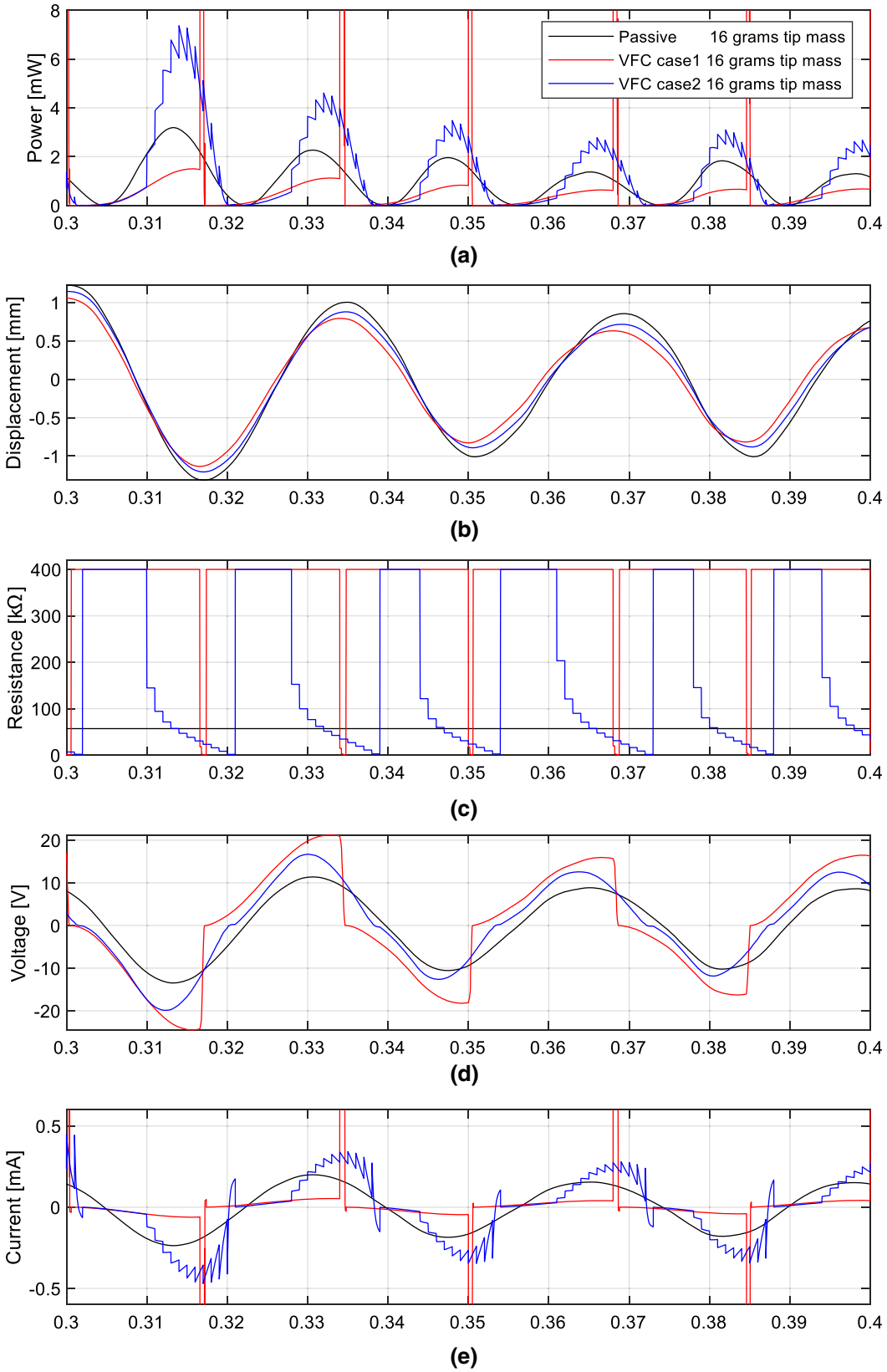

Fig. 16 Dynamic performance of the piezoelectric with 16 g tip mass: power storage (**a**), tip displacement (**b**), resistance (**c**), voltage (**d**) and current (**e**) by comparing passive versus VFC controls

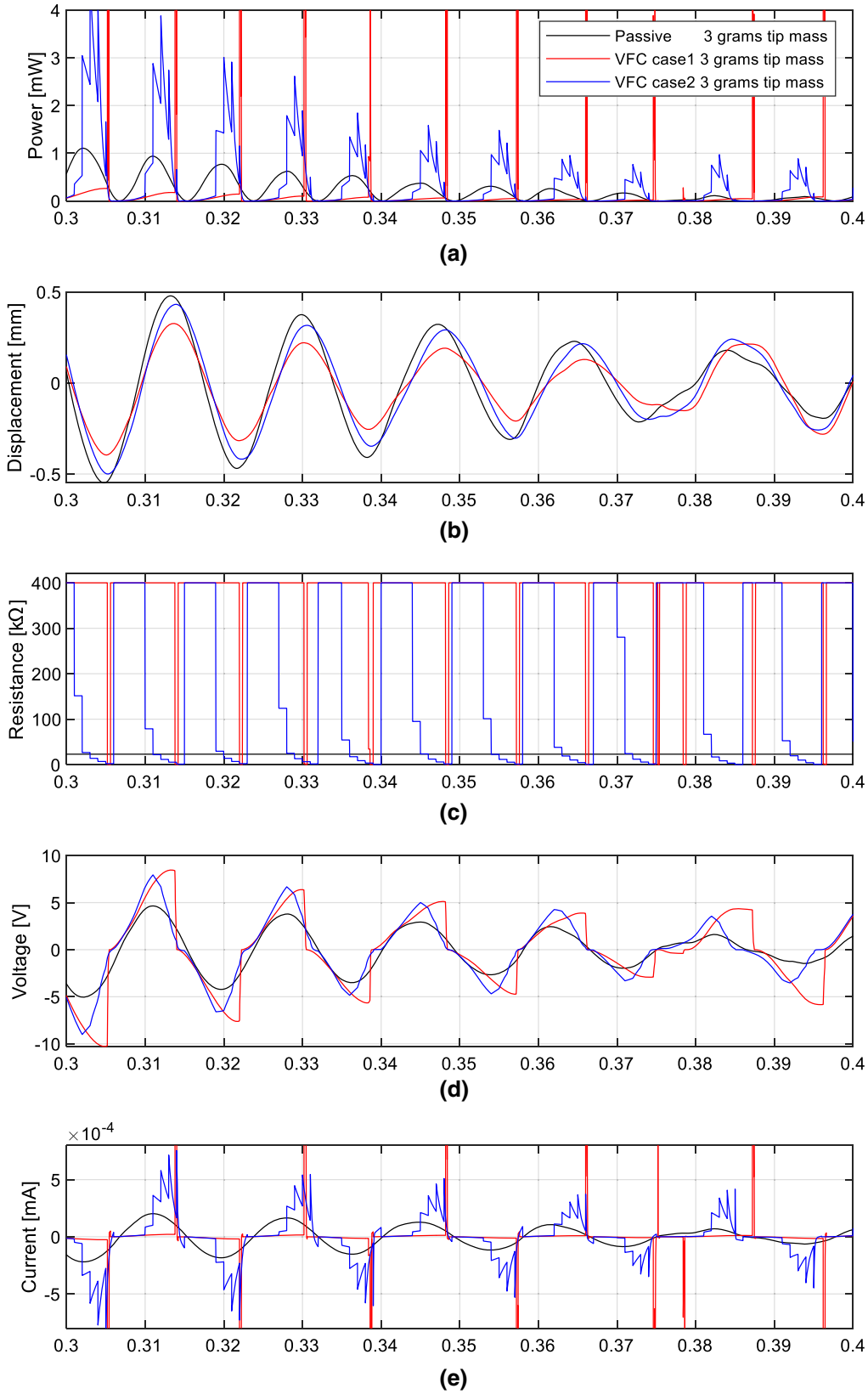

Fig. 17 Dynamic performance of the piezoelectric with 3 g tip mass: power storage (**a**), tip displacement (**b**), resistance (**c**), voltage (**d**) and current (**e**) by comparing passive vs VFC controls

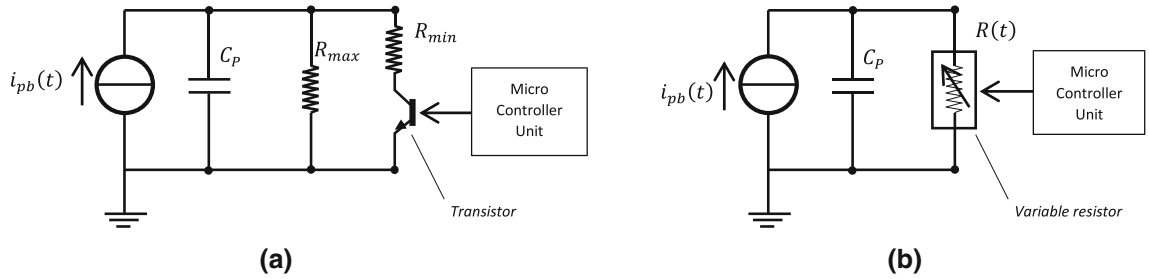

Fig. 18 Circuit diagram with switch transistor (**a**) and variable resistance (**b**)

C*ase 2* shows a much lower RMS power, similarly to the passive trend, with the advantage of a much smoother control action. In fact, unlike the previous strategy, it requires much slower electronics to manage the energy storage and no need for any fast capacitor. On a contrary, a more sophisticated control circuit to manage a variable resistor is required that can be implemented via operational amplifiers as sketched in Fig. 18b.

From Table 2, it follows the energy stored by the NMPC control is almost 2–2.3 times greater than the passive case for the two tip masses, maintaining a low peak-peak displacement and a moderate RMS power value. NMPC control is used only to determine an upper bound for the energy harvested, and cannot be used for a real feedback control for piezoelectric systems, because the solution times for predict a few milli-seconds stand on the tens of seconds for an Intel i7 of 11th generation.

Moreover, it is important to note that the total energy stored must necessarily be subtracted from the energy spent to perform the measure and the power supply of the controller. On the electronic market, micro accelerometers, as well as strain gauge sensors, can be found with low consumption, around μW, as referred in [50–52]. In addition to the use of sensors, a low consumption microcontroller is required to control the resistance of the electrical circuit and apply the control law thanks to an analog–digital converter. Inside the microcontroller, it will be possible to implement a state observer, for example, an extended Kalman filter or other methods [53, 54], to correctly estimate the variables necessary for the application of the control law.

As an example, $1.67J$ can be harvested, considering 10 min of *VFC case1* with 16 g piezo-beam tip mass, of about $20grams$ overall weight on board of a SMART car, located in the engine compartment (see Fig. 12b). The order of magnitude of the expected power is $\frac{1.67J}{600\text{s}} \approx 2.8\text{mW}$ and the specific power is about 140mW/kg where the weight of the electronic board and sensors is roughly supposed to be 1 g for each piezo-beam device. The electronic board, from an electrical engineering point of view, should read data sensors, vary the resistors and converting the alternating voltage output via operational circuits.

Finally, Fig. 19 shows the energy extracted along 10 min of simulation, for all the cases analyzed above, therefore proving the abilities of the control VFC is a valid alternative to the passive system.

6 Final remarks and conclusion

This paper investigates the upper bound of the energy that can be harvested by piezoelectric devices installed on the board of cars. To this aim, a commercial harvester has been selected, experimentally tested, and a harvester model has been developed and tuned using experimental results. Moreover, a small urban car has been tested to acquire the vibration spectra at different locations, where it is meaningful to install the energy harvesters.

The performance of the commercial harvester is boosted by using an adaptive impedance control of its resistive part. This operation is obtained by applying a novel control method recently proposed by the authors, the Variational Feedback Control (VFC).

Classical methods of passive energy harvesting are often based on resonance effects, but the high sensitivity of the output power to the external frequency excitation induces poor performances in the presence of a wide spectrum excitation. Semi-active energy harvesters are generally based on empirical control law; instead, in this paper, VFC introduces a rationale for a smart adaptive mechanism with the explicit and strict target of maximizing the output power. The vibrations coming from the rough road, crossing bumps, road holes, and the internal combustion engine become suitable sources of energy that can be converted into electrical energy through an array of vibrating piezo harvesters.

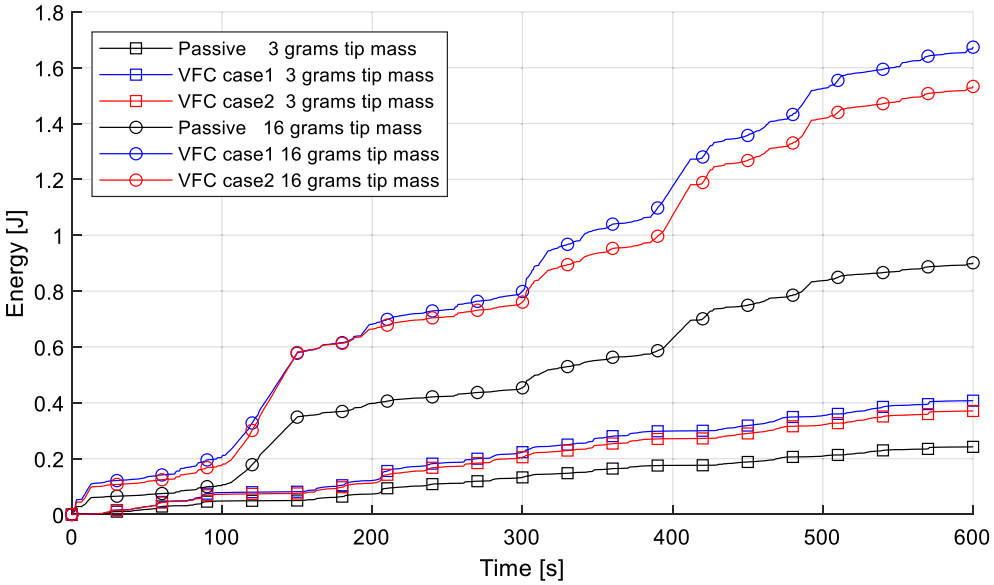

Fig. 19 Comparison of accumulated energy for 10 min of simulation

With lightweight instrumentation it is possible to obtain, using the semi-adaptive impedance method presented in this paper, a power output of about 2.8mW for the single piezo-beam, with an order of magnitude of the power density upper bound of about 140mW/kg.

These reference numbers help in the analysis of the energy convenience of these devices to be installed on board.

In fact, the weight of the harvester and related electronics is carried by the car implying extra-energy costs, because the more the weight on the tires, the more the tire resistance. On the other hand, the harvester can be placed very close to the energy user unit, because of its small dimensions, with the beneficial effect of reducing the cables weight.

An additional element of evaluation is represented by the simplicity of the algorithms used to control the harvester. The NMPC controllers are not feasible to this aim, and NMPC is used in the previous sections only to determine the technical upper bound for the harvester power. In fact, the algorithm requires computational times that are not compatible with the real-time use of the device. VFC has indeed a practical chance of implementation, being a very simple feedback control, fast enough and at the same time guaranteeing a doubling of the extracted power with respect to a passive harvester. These elements take all part into a power balance that would drive the choice of installing or not the harvesters on board.

The transport cost per their unit weight on board can be estimated using the following simple method. In fact, the cost of transport in terms of power depends on the equivalent friction coefficient of the tire $f(v)$, that is a function of the velocity of the car v (it increases as the speed increases), see Fig. 20. The normal load applied to the tire is N, and the average dissipated power due to the tire rolling is:

$$Nf(v)v \tag{30}$$

where $Nf(v)$ represents the horizontal resistance force of the tire, and $f(v)v$ the power of transport per unit weight. If the additional weight of the harvester is ΔN_H and ΔN_C is the cable weight saving, the differential average dissipated power is $f(v)v(\Delta N_H - \Delta N_C)$ and the condition to verify to have some convenience in installing the harvester is clearly:

$$P_H > f(v)v(\Delta N_H - \Delta N_C) \tag{31}$$

where P_H is the average power produced by the harvester.

Note that this condition depends on the velocity of the car. This means that for an average use of the car at low speed, typically in urban driving conditions, the energy convenience is reasonably larger. Moreover, the road roughness of urban roads is higher than on highways, and the vibration level on board is stronger, pumping more power into the harvester. On flat roads at high speed, we can expect the system is less convenient.

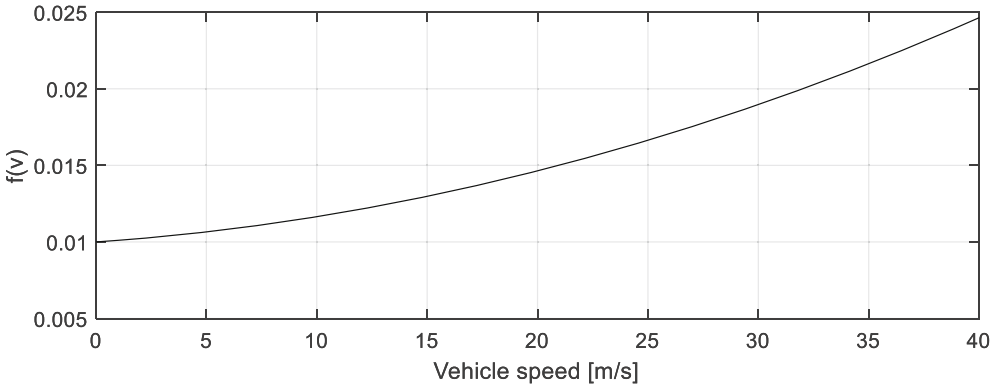

Fig. 20 Coefficient of friction $f(v)$ due to the rolling resistance of a standard utility car

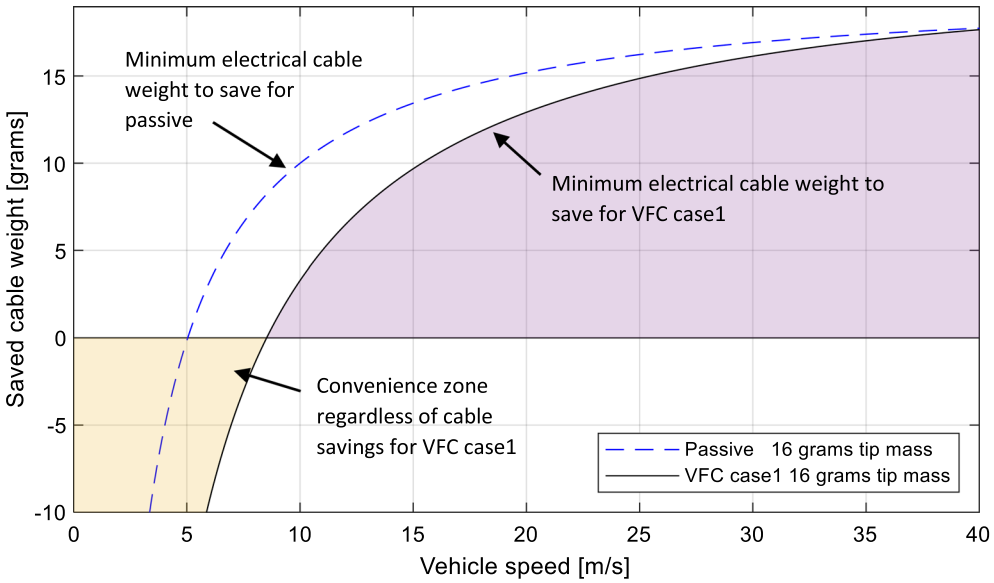

Fig. 21 Quantity diagram of minimum weight to be saved in terms of electrical wiring inside the vehicle

The previous inequality can be a reference to estimate the cable weight saving one needs to accept to install the harvesters system on board:

$$\Delta N_C > \Delta N_H - \frac{P_H}{f(v)v} \tag{32}$$

As a final remark, note that in modern automotive technology the cables are an important issue. In fact, their saving is important for decarbonization. In a medium car, there are more than $60kg$ of cable weight, with total lengths of more than several kilometers. Energy harvesting can be one of support for a reduction of this weight.

Fig. 21 shows the trend of Eq. (32) for the case controlled by VFC case1 compared to the passive case with an added mass of 16 g. The axis of the ordinates shows the minimum wiring weight ΔN_C to be saved for a convenient use of the harvester. Negative values for ΔN_C means it is convenient to install the piezoelectric system on site, whatever the wiring weight, as it happens in the low-speed range. The branch of the curve for positive values of ΔN_C shows the minimum amount of wiring weight saving that made it convenient the use of the energy harvester.

Funding Open access funding provided by Università degli Studi di Roma La Sapienza within the CRUI-CARE Agreement.

Declarations

Conflict of interest On behalf of all authors, the corresponding author states that there is no conflict of interest.

References

1. Priya, S., Inman, D.J.: Energy Harvesting Technologies. Springer, US (2008)
2. Kaltenbacher, B., Krejčí, P.: Analysis of an optimization problem for a piezoelectric energy harvester. Arch. Appl. Mech. **89**(6), 1103–1122 (2019). https://doi.org/10.1007/s00419-018-1459-6
3. Erturk, A., Inman, D.: An Experimentally Validated Bimorph Cantilever Model for Piezoelectric Energy Harvesting from Cantilevered Beams, pp. 25009–25018 (2009)
4. Shu, Y.C., Lien, I.C.: Analysis of power output for piezoelectric energy harvesting systems, p. 1499 (2006).
5. Dicken, J., Mitcheson, P.D., Stoianov, I., Yeatman, E.M.: Power-extraction circuits for piezoelectric energy harvesters in miniature and low-power applications. IEEE Trans. Power Electron. **27**(11), 4514–4529 (2012). https://doi.org/10.1109/TPEL.2012.2192291
6. Hulst, R.D., Driesen, J.:Power processing circuits for vibration-based energy harvesters, In: 2008 IEEE Power Electronics Specialists Conference, pp. 2556–2562. (2008). https://doi.org/10.1109/PESC.2008.4592325.
7. Shu, Y.C., Lien, I.C., Wu, W.J.: An improved analysis of the SSHI interface in piezoelectric energy harvesting. Smart Mater. Struct. **16**(6), 2253 (2007)
8. Cossalter, V., Doria, A., Garbin, S., Lot, R.: Frequency-domain method for evaluating the ride comfort of a motorcycle. Veh. Syst. Dyn. **44**(4), 339–355 (2006). https://doi.org/10.1080/00423110500420712
9. Orfei, F., Vocca, H., Gammaitoni, L.: Linear and non linear energy harvesting from bridge vibrations. pp. V008T10A054 (2016), https://doi.org/10.1115/DETC2016-59650.
10. Zhou, M., Zhao, H.: Revisit to the theoretical analysis of a classical piezoelectric vibration energy harvester. Arch. Appl. Mech. **90**(11), 2379–2395 (2020). https://doi.org/10.1007/s00419-020-01727-x
11. Kaźmierski, T.J., Beeby, S.: Energy Harvesting Systems: Principles, Modeling and Applications (SpringerLink : Bücher). Springer, New York (2010)
12. Nazemizadeh, M., Bakhtiari-Nejad, F., Assadi, A., Shahriari, B.: Size-dependent nonlinear dynamic modeling and vibration analysis of piezo-laminated nanomechanical resonators using perturbation method. Arch. Appl. Mech. **90**(8), 1659–1672 (2020). https://doi.org/10.1007/s00419-020-01678-3
13. Paknejad, A., Rahimi, G., Salmani, H.: Analytical solution and numerical validation of piezoelectric energy harvester patch for various thin multilayer composite plates. Arch. App. Mech. **88**(7), 1139–1161 (2018). https://doi.org/10.1007/s00419-018-1363-0
14. Doria, A., Medè, C., Fanti, G., Desideri, D., Maschio, A., Moro, F.: Development of Piezoelectric Harvesters with Integrated Trimming Devices. p. 557 (2018)
15. Dhote, S., Yang, Z., Zu, J.: Modeling and experimental parametric study of a tri-leg compliant orthoplanar spring based multi-mode piezoelectric energy harvester. Mech. Syst. Signal Process. (2018). https://doi.org/10.1016/j.ymssp.2017.04.031
16. Viet, N.V., Zaki, W., Umer, R.: Analytical investigation of an energy harvesting shape memory alloy–piezoelectric beam. Arch. Appl. Mech. **90**(12), 2715–2738 (2020). https://doi.org/10.1007/s00419-020-01745-9
17. Mojrzisch, S., Twiefel, J.: Phase-controlled frequency response measurement of a piezoelectric ring at high vibration amplitude. Arch. Appl. Mech. **86**(10), 1763–1769 (2016). https://doi.org/10.1007/s00419-015-1032-5
18. Ramlan, R., Brennan, M.J., Mace, B.R., Burrow, S.G.: On the performance of a dual-mode non-linear vibration energy harvesting device. J. Intell. Mater. Syst. Struct. **23**(13), 1423–1432 (2012). https://doi.org/10.1177/1045389X12443017
19. Castagnetti, D., Radi, E.: A piezoelectric based energy harvester with dynamic magnification: modelling, design and experimental assessment. Meccanica **53**(11–12), 2725–2742 (2018). https://doi.org/10.1007/s11012-018-0860-0
20. De Pasquale, G.: Artificial human joint for the characterization of piezoelectric transducers in self-powered telemedicine applications. Meccanica **51**(9), 2259–2275 (2016). https://doi.org/10.1007/s11012-016-0359-5
21. Syta, A., Bowen, C.R., Kim, H.A., Rysak, A., Litak, G.: Experimental analysis of the dynamical response of energy harvesting devices based on bistable laminated plates. Meccanica **50**(8), 1961–1970 (2015). https://doi.org/10.1007/s11012-015-0140-1
22. Xia, G., Fang, F., Wang, Q., Zhang, M., Wang, J.: "Performance analysis of piezoelectric energy harvesters with a tip mass and nonlinearities of geometry and damping under parametric and external excitations. Arch. Appl. Mech. (2020). https://doi.org/10.1007/s00419-020-01721-3
23. Xia, G., Fang, F., Zhang, M., Wang, Q., Wang, J.: Performance analysis of parametrically and directly excited nonlinear piezoelectric energy harvester. Arch. Appl. Mech. **89**(10), 2147–2166 (2019). https://doi.org/10.1007/s00419-019-01568-3
24. Ottman, G.K., Hofmann, H.F., Bhatt, A.C., Lesieutre, G.A.: Adaptive piezoelectric energy harvesting circuit for wireless remote power supply. IEEE Trans. Power Electron. **17**(5), 669–676 (2002). https://doi.org/10.1109/TPEL.2002.802194

25. Guyomar, D., Lallart, M.: Recent progress in piezoelectric conversion and energy harvesting using nonlinear electronic interfaces and issues in small scale implementation. Micromachines (2011). https://doi.org/10.3390/mi2020274
26. Lefeuvre, E., Badel, A., Brenes, A., Seok, S., Woytasik, M., Yoo, C.S.: Analysis of piezoelectric energy harvesting system with tunable SECE interface. Smart Mater. Struct. **26**(3), 035065 (2017)
27. Singh, K.B., Bedekar, V., Taheri, S., Priya, S.: Piezoelectric vibration energy harvesting system with an adaptive frequency tuning mechanism for intelligent tires. Mechatronics **22**(7), 970–988 (2012). https://doi.org/10.1016/j.mechatronics.2012.06.006
28. Pepe, G., Carcaterra, A.: VFC—variational feedback controller and its application to semi-active suspensions. Mech. Syst. Signal Process. (2016). https://doi.org/10.1016/j.ymssp.2016.01.002
29. Pepe, G., Roveri, N., Carcaterra, A.: "Prototyping a new car semi-active suspension by variational feedback controller," In: Proceedings of ISMA 2016 - International Conference on Noise and Vibration Engineering and USD2016 - International Conference on Uncertainty in Structural Dynamics, pp. 231–245 (2016) [Online]. Available: https://www.scopus.com/inward/record.uri?eid=2-s2.0-85018191875&partnerID=40&md5=e88d23db689766f93f188de213fecf39
30. Pepe, G., Carcaterra, A.: Semi-active damping by variational control algorithms. Proc. Int. Conf. Struct. Dyn. EURODYN **2014**, 1721–1727 (2014)
31. Antonelli, D., Nesi, L., Pepe, G., Carcaterra, A.: "Mechatronic control of the car response based on VFC," In: Proceedings of ISMA 2018 - International Conference on Noise and Vibration Engineering and USD 2018 - International Conference on Uncertainty in Structural Dynamics, pp. 79–92 (2018). [Online]. Available: https://www.scopus.com/inward/record.uri?eid=2-s2.0-85060373090&partnerID=40&md5=ec5b75ae9b9810199c512bef66e38b56
32. Pepe, G., Antonelli, D., Nesi, L., Carcaterra, A.: "Flop: Feedback local optimality control of the inverse pendulum oscillations," In: Proceedings of ISMA 2018 - International Conference on Noise and Vibration Engineering and USD 2018 - International Conference on Uncertainty in Structural Dynamics, pp. 93–106 (2018). [Online]. Available: https://www.scopus.com/inward/record.uri?eid=2-s2.0-85060389675&partnerID=40&md5=d29242dd2913e82530da27cdf6ac222a
33. Paifelman, E., Pepe, G., Carcaterra, A.: An optimal indirect control of underwater vehicle. Int. J. Control (2019). https://doi.org/10.1080/00207179.2019.1590737
34. Antonelli, D., Nesi, L., Pepe, G., Carcaterra, A.: A novel approach in optimal trajectory identification for autonomous driving in racetrack. 2019 18th Eur. Control Conf. ECC (2019). https://doi.org/10.23919/ECC.2019.8795637
35. Rojas, R.A., Carcaterra, A.: An approach to optimal semi-active control of vibration energy harvesting based on MEMS. Mech. Syst. Signal Process. **107**, 291–316 (2018). https://doi.org/10.1016/j.ymssp.2017.11.005
36. Midé. https://www.mide.com/ (accessed.
37. Timoshenko, S.: Vibration Problems in Engineering—Scholar's Choice Edition. Scholar's Choice (2015).
38. Erturk, A., Inman, D.J.: Piezoelectric Energy Harvesting. Wiley (2011).
39. Doria, A., Moro, F., Desideri, D., Maschio, A., Zhang, Z.: An Impulsive Method for the Analysis of Piezoelectric Energy Harvesters for Intelligent Tires, pp. V003T01A025 (2016), https://doi.org/10.1115/DETC2016-59105.
40. Paifelman, E., Pepe, G., La Gala, F., Carcaterra, A.:Control of fluctuations of a tethered unmanned-underwater-vehicle," In: Proceedings of ISMA 2018 - International Conference on Noise and Vibration Engineering and USD 2018 - International Conference on Uncertainty in Structural Dynamics, pp. 241–251 (2018). [Online]. Available: https://www.scopus.com/inward/record.uri?eid=2-s2.0-85060396810&partnerID=40&md5=c05d3e8126be9cb8cf5d96cd3e144633
41. Pepe, G., Carcaterra, A.:"A new semi-active variational based damping control," In: MESA 2014-10th IEEE/ASME International Conference on Mechatronic and Embedded Systems and Applications, Conference Proceedings (2014). [Online]. Available: http://www.scopus.com/inward/record.url?eid=2-s2.0-84911969901&partnerID=40&md5=3611145674b6d640dae8ba6b918382fa
42. Pepe, G., Carcaterra, A.: "Semi-active damping by variational control algorithms, In: Presented at the Proceedings of the 9th International Conference on Structural Dynamics, EURODYN 2014, Porto, Portugal (2014). [Online]. Available: http://paginas.fe.up.pt/~eurodyn2014//CD/papers/240_MS09_ABS_1721.pdf.
43. Pepe, G., Carcaterra, A., Giorgio, I., Del Vescovo, D.: Variational Feedback Control for a nonlinear beam under an earthquake excitation. Math. Mech. Solids (2014). https://doi.org/10.1177/1081286514562878
44. Bryson, A. E.: Applied Optimal Control: Optimization, Estimation and Control (Halsted Press book'). Taylor & Francis (1975).
45. Vikhar, P. A.: "Evolutionary algorithms: A critical review and its future prospects," In: 2016 International Conference on Global Trends in Signal Processing, Information Computing and Communication (ICGTSPICC), pp. 261–265 (2016), https://doi.org/10.1109/ICGTSPICC.2016.7955308.
46. Grüne, L., Pannek, J.: Nonlinear Model Predictive Control. In: Grüne, L., Pannek, J. (eds.) Nonlinear Model Predictive Control: Theory and Algorithms, pp. 45–69. Springer International Publishing, Cham (2017)
47. Koryakovskiy, I., et al.: Benchmarking model-free and model-based optimal control. Robot. Auton. Syst. **92**, 81–90 (2017). https://doi.org/10.1016/j.robot.2017.02.006
48. Quirynen, R., Berntorp, K., Kambam, K., Di Cairano, S.: Integrated Obstacle Detection and Avoidance in Motion Planning and Predictive Control of Autonomous Vehicles, In 2020 American Control Conference (ACC), pp. 1203–1208 (2020) https://doi.org/10.23919/ACC45564.2020.9147820.
49. Richalet, J., Rault, A., Testud, J.L., Papon, J.: Model predictive heuristic control: applications to industrial processes. Automatica **14**(5), 413–428 (1978). https://doi.org/10.1016/0005-1098(78)90001-8
50. Bazghaleh, M., Grainger, S., Mohammadzaheri, M.: A review of charge methods for driving piezoelectric actuators. J. Intell. Mater. Syst. Struct. **29**(10), 2096–2104 (2017). https://doi.org/10.1177/1045389X17733330
51. Abreu, G.L.C.M., Ribeiro, J.F., Steffen, V., Jr.: Experiments on optimal vibration control of a flexible beam containing piezoelectric sensors and actuators. Shock Vib. **10**(5–6), 283–300 (2003)
52. Lu, E., Li, W., Yang, X., Fan, M., Liu, Y.: modelling and composite control of single flexible manipulators with piezoelectric actuators. Shock Vib. **2016**, 2689178 (2016). https://doi.org/10.1155/2016/2689178

53. Zhang, X., Dong, Z., Faria, C., Hengster-Movric, K., Desmet, W.: Observer-Based Distributed Controllers Design for a Cantilever Beam, In: Cham, E., Wee, S. (eds.) Sensors and Instrumentation, vol. 5, pp. 163–170, Springer International Publishing (2016).
54. Vatankhah, R., Karami, F., Salarieh, H.: Observer-based vibration control of non-classical microcantilevers using extended Kalman filters. Appl. Math. Modell. **39**(19), 5986–5996 (2015). https://doi.org/10.1016/j.apm.2015.01.047